Planetary and Space Science 57 (2009) 1699–1705

Contents lists available at ScienceDirect

Planetary and Space Science

journal homepage: www.elsevier.com/locate/pss

Response of Saturn's ionosphere to solar radiation: Testing parameterizations for thermal electron heating and secondary ionization processes

Luke Moore [a,*], Marina Galand [b], Ingo Mueller-Wodarg [b], Michael Mendillo [a]

[a] Center for Space Physics, Boston University, Boston MA 02215, United States
[b] Imperial College London, London, UK

ARTICLE INFO

Article history:
Received 15 November 2008
Received in revised form
10 April 2009
Accepted 5 May 2009
Available online 12 May 2009

Keywords:
Saturn
Ionosphere
Photoelectron heating
Secondary ionization
Modeling

ABSTRACT

We evaluate the effectiveness of two parameterizations in Saturn's ionosphere over a range of solar fluxes, seasons, and latitudes. First, the parameterization of the thermal electron heating rate, Q^*_e, introduced in [Moore, L., Galand, M., Mueller-Wodarg, I., Yelle, R.V., Mendillo, M., 2008. Plasma temperatures in Saturn's ionosphere. J. Geophys. Res. 113, A10306. doi:10.1029/2008JA013373.] for one specific set of conditions, is found to produce ion and electron temperatures that agree with self-consistent suprathermal electron calculations to within 2% on average under all conditions considered. Next, we develop a new parameterization of the secondary ion production rate at Saturn based on the calculations of [Galand, M., Moore, L., Mueller-Wodarg, I., Mendillo, M., 2009. Modeling the photoelectron secondary ionization process at Saturn. accepted. J. Geophys. Res.]; it is found to be accurate to within 4% on average. The demonstrated effectiveness of these two parameterizations over a wide range of input conditions makes them good candidates for inclusion in 3D Saturn thermosphere–-ionosphere general circulation models (TIGCMs).

1. Introduction

This paper presents modeling results associated with two ionospheric processes that have received relatively little attention at Saturn until recently: (1) thermal electron heating, and (2) secondary electron impact ionization induced by suprathermal photoelectrons. To address the remaining discrepancies between theory and observation in Saturn's ionosphere, it is important that both of the above processes be accounted for adequately. Ion and electron temperatures alter the topside scale height of the ionosphere (Moore et al., 2008), and play an important role in determining the transfer of plasma between an ionosphere and magnetosphere (e.g., Miller et al., 2005; Schunk and Nagy, 1978). Secondary ionization enhances the peak electron density by as much as ~30% and increases the electron density of the lower ionosphere by up to an order of magnitude (Galand et al., 2009). Furthermore, the altitude region over which secondary ionization is important at Saturn is also the region where the bulk of the ionospheric Pedersen conductance is produced (Moore et al., 2004) – a key parameter in ionosphere–magnetosphere coupling (e.g., Cowley et al., 2008, and references therein). Finally, the high-degree of vertical structuring observed in all radio occultations of Saturn below the electron density peak requires further theoretical explanation (Atreya et al., 1984; Nagy et al., 2006; Kliore et al., 2009). One possible explanation for this structuring is that upward propagating gravity waves perturb the lower ionosphere (Matcheva et al., 2001), a region where secondary production is dominant over primary production (<~1000 km; Galand et al., 2009).

Estimating the state and evolution of the upper atmosphere on a global scale requires a thermosphere–ionosphere global circulation model (TIGCM), a three-dimensional time-dependent solution to the non-linear Navier–Stokes equations of continuity, momentum, and energy. TIGCMs are typically computationally intensive, and usually proceed slower than real time (e.g., Achilleos et al., 1998; Bougher et al., 2005). While the power of modern computers is beginning to ameliorate this issue somewhat, there will always remain physical processes that require parameterization within such a model. For instance, modern terrestrial TIGCMs often utilize a simple parameterization (Swartz and Nisbet, 1972) of the thermal electron heating rate (e.g., Roble et al., 1987; Millward et al., 1996), and frequently parameterize the secondary ionization rate as well (Richards and Torr, 1988; Lilensten et al., 1989; Titheridge, 1996). Our goals here are (1) to develop a parameterization of the secondary ionization rate for inclusion in a Saturn TIGCM, and (2) to assess the reliability of both this parameterization and a parameterization of the thermal electron heating rate (Moore et al., 2008) over a range of latitudes, seasons, and solar flux inputs.

* Corresponding author. Tel.: +1 617 9539064.
E-mail address: moore@bu.edu (L. Moore).

0032-0633/$ - see front matter © 2009 Elsevier Ltd. All rights reserved.
doi:10.1016/j.pss.2009.05.001

2. Approach

This study presents results from simulations that involve a series of coupled one-dimensional models, described below. The benefit of 1D over 3D, in this case, is that it allows for a large number of simulations to create and test parameterizations for Saturn's ionosphere. Furthermore, the 1D model ionosphere used here comes from the development of STIM – the Saturn Thermosphere–Ionosphere Model – a suite of 1D, 2D, and 3D models of Saturn's upper atmosphere that have been compared with observations by Cassini (Moore et al., 2006; Moore and Mendillo, 2007) and Voyager (Mendillo et al., 2005; Moore et al., 2008).

2.1. Solar flux input

Any atmospheric model requires accurate solar flux inputs, and particularly EUV and soft X-ray fluxes in the case of the ionosphere. At Earth, the quality of available irradiance observations and estimations has steadily increased with time, as more satellite data becomes available and more sophisticated empirical models are developed that incorporate such data. At Saturn, we must rely upon adjusted terrestrial fluxes, which often involve some degree of extrapolation as Saturn and Earth rarely see the same hemisphere of the Sun at the same time. The extrapolation used here to go from the solar flux measured or estimated at Earth to the solar flux incident at the top of Saturn's atmosphere takes into account both the distance correction (i.e., going from 1 to ~9.5 AU) and the phasing over time (i.e., the correction for Earth and Saturn being at different solar longitudes).

This study evaluates two of the most commonly used empirical models of solar irradiance: Solar2000 (Tobiska et al., 2000; Tobiska and Bouwer, 2006) and EUVAC (Richards et al., 1994a, 1994b). The EUV flux model for aeronomic calculations (EUVAC) is based on the F74113 reference spectrum (Heroux and Higgins, 1977; Torr et al., 1979) and the solar cycle variation of the flux measured by the Atmosphere Explorer E (AE-E) satellite (Hinteregger et al., 1981). Solar2000 receives continuous updates (http://www.spacewx.com/solar2000.html), and incorporates data from more than a dozen rockets and satellites to estimate the solar irradiance for any day from 1947 to the present.

In addition to these two empirical models, we make direct use of data from the Solar EUV Experiment (SEE) aboard the NASA Thermosphere Ionosphere Mesosphere Energetics and Dynamics (TIMED) mission (Woods et al., 2005), which has measured the solar XUV, EUV, and FUV irradiance from 2002 to the present (http://lasp.colorado.edu/see/). The SEE observations are a major driver of Solar2000, and so Solar2000 and SEE solar fluxes are nearly identical for periods where SEE data are available (and over SEE's 0.5–194.5 nm wavelength range).

2.2. Saturn's ionosphere

As Saturn's upper atmosphere is predominantly composed of molecular hydrogen, the production of H_2^+ accounts for ~90% of the photoionization in the ionosphere, followed by H^+ (~9%) and He^+ (~1%). However, H_2^+ is converted into H_3^+ through charge exchange with molecular hydrogen nearly as quickly as it is produced. The relatively fast dissociative recombination of H_3^+ with electrons – with a lifetime of order 1000 s near the ionospheric peak – means the molecular ion density in Saturn's ionosphere closely follows the solar zenith angle, with a maximum shortly after noon and a minimum before dawn. At dusk, H_3^+ is enhanced over the dawn values, as there is an additional source of H_2^+ (and hence, H_3^+) due to the charge exchange of H^+ and H_2 (Moore et al., 2004). The radiative recombination of protons, on the other hand, is extremely slow, which, combined with the short Saturn day (~10.7 h), means the H^+ density continues to build up to a constant diurnal value of $\sim 10^5\,cm^{-3}$ unless alternative loss pathways are introduced. Those pathways typically take the form of (1) a charge exchange reaction between H^+ and vibrationally excited H_2 (McElroy, 1973; McConnell et al., 1982), and (2) a charge exchange between H^+ and the water influx from Saturn's rings and icy satellites (Connerney and Waite, 1984). Near the homopause, H_3^+ and H^+ charge exchange with hydrocarbons, primarily methane, contributing to a complex hydrocarbon ion ledge at the bottomside of the ionosphere (Moses and Bass, 2000; see also Kim and Fox, 1994). Therefore, the "steady-state" theoretical picture of Saturn's background ionosphere is one in which H^+ dominates the topside with little diurnal variation, while H_3^+ and hydrocarbon ions dominate near and below the electron density peak with strong diurnal variation.

In Fig. 1, we present a summary of STIM results for the Saturn thermosphere and ionosphere. Each panel presents physical quantities resulting from self-consistent TIGCM runs, or from the physics-based 1D calculations that rely on TIGCM output for the initial conditions, as described above. In addition, several quantities resulting from parameterizations for the thermal electron heating rate (Moore et al., 2008) and the secondary production rate (described below) in Section 3.2 are included in panels (e)–(f) and (b)–(c), respectively.

2.3. Modeling description

To reproduce the behavior described above, we couple a series of three 1D models designated here as: thermosphere, ionosphere, and suprathermal electron transport. The thermosphere model extends from 5×10^{-3} mbar (around 590 km above the 1 bar level) to around 10^{-11} mbar (~3000 km) and contains the principal gases H, H_2, and He, as well as CH_4. A diffusive equilibrium distribution is assumed, which was calculated with a 1D diffusion model derived from the 3D STIM (1D providing the benefit of increased vertical resolution and a reduced lower boundary), using an eddy diffusion coefficient identical to that of Moses et al. (2000a), placing the CH_4 homopause near the 1.3×10^{-5} mbar level (altitude of ~800 km). The CH_4 mixing ratios are a good fit to observations as reviewed by Moses et al. (2000a). We assume a thermal profile consistent with observations by Smith et al. (1983) and Hubbard et al. (1997), with exospheric temperatures (above the 2×10^{-7} mbar level) of 420 K and temperatures in the mesosphere (below the 10^{-4} mbar level) constant at 136 K. In addition, a steady-state influx of water at the top of the atmosphere of $5\times10^6\,cm^{-2}\,s^{-1}$ is used to obtain neutral water densities. This flux is within the boundaries of previous estimates (e.g., Connerney and Waite, 1984; Moses et al., 2000b), and represents only a fraction of the possible geyser source at Enceladus (e.g., Porco et al., 2006). The thermosphere remains as a constant background throughout the rest of the calculations.

Based on this thermosphere, the 1D ionospheric module solves the equations of ion continuity, momentum, and energy using the methods and rates described by Moore et al. (2004, 2008). Specifically, the ionosphere is solved via explicit time integration, includes a treatment of attenuation of sunlight by Saturn's rings (not used in this study), and adopts the Moses and Bass (2000) estimation of reaction k_1, the charge exchange between H^+ and vibrationally excited H_2. Though we use the Moses and Bass (2000) method of estimating k_1, the reaction rates used are 25% of the Moses and Bass values. Thus, due to the altitude dependence of the H_2 vibrational states, our k_1 reaction rate here is 2×10^{-14}

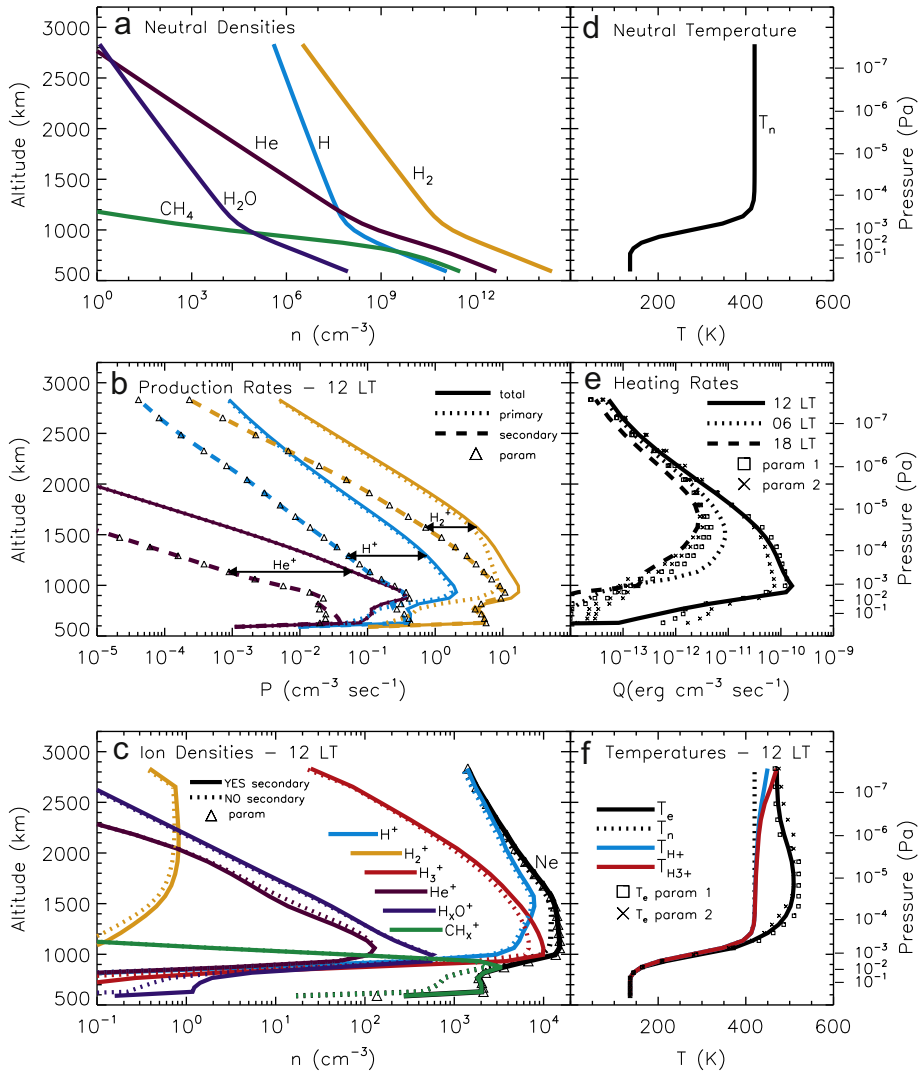

Fig. 1. Saturn Thermosphere-Ionosphere Model (STIM) results for 30° N latitude, using TIMED/SEE solar maximum conditions (20 October, 2002) during Saturn equinox. Note that 0 km altitude corresponds to the 1 bar pressure level. (a) Background neutral densities. (b) Primary (dotted), secondary (dashed), and total (solid) production rates at local noon for H^+, H_2^+, and He^+, where the H^+ production is the sum of direct photoionization of H and dissociative photoionization of H_2. In addition, the triangles represent secondary production rates derived from the secondary ionization parameterization described in Section 3.2. (c) Ion and electron densities at local noon. Solid curves represent calculations that have accounted for secondary production, while dotted curves represent calculations that have not. Triangles give the electron density that results from the parameterizations of the secondary production rates described in Section 3.2. (d) Background neutral temperature. (e) Thermal electron heating rates at local noon (solid line), dawn (dotted line), and dusk (dashed line). In addition, the cross and square symbols represent heating rates estimated from two different parameterizations (Section 3.1; also, Moore et al., 2008). (f) Ion and electron temperatures at local noon. The cross and square symbols correspond to electron temperatures that have been derived using the two different parameterizations of the electron heating rates.

$cm^{-3}\,s^{-1}$ above 2000 km, and ranges from (0.2 to 200) $\times 10^{-16}$ $cm^{-3}\,s^{-1}$ below. This reduction is due to two factors: (1) the assertion by Huestis (2008) that there is additional vibrational relaxation of H_2 that has not been accounted for in previous derivations, and (2) the fact that a water influx of the magnitude estimated from Voyager era (e.g., Jurac and Richardson, 2005) and Cassini era (Johnson et al., 2006) sources is capable of depleting the ionospheric electron density to observed levels (Moore et al., 2006).

The results of the ionospheric module – electron density and ion and electron temperature as functions of time and altitude – serve as input for a suprathermal electron transport code applied to photoelectrons and secondary electrons. This suprathermal electron code utilizes a multistream approach for solving the Boltzmann equation, and provides estimates for the secondary ion production rates and for the heating rates of the ambient, thermal electrons (Moore et al., 2008; Galand et al., 2009). These inputs then drive plasma temperatures and ionospheric densities within the ionospheric module, perturbing the initial ionosphere, and providing a new background to the suprathermal electron code. The ambient electron gas is heated by energetic photoelectrons; electron–ion Coulomb collisions, plasma-neutral collisions, and vertical heat transport cool the electron and ion gases (Moore et al., 2008). The coupling process between the ionospheric and suprathermal electron codes is repeated until convergence is reached, which typically occurs after two iterations.

3. Results

This study analyzes the effectiveness of two different parameterizations over the range of different simulation conditions given in Table 1. The specific equations for the parameterizations of the secondary production rate and the thermal electron heating rate – both based on the primary photoionization rate – are given in Appendix A; their accuracy and variability are described below.

3.1. Electron heating

A parameterization of the thermal electron heating rate at Saturn has previously been developed that is able to reproduce the heating rate calculated within the suprathermal electron routine to within a few percent at all local times and altitudes (Eq. (A2); Moore et al., 2008). The square symbols in Fig. 1e illustrate the good agreement between the full simulation and this parameterization ("param 1", which uses the noontime electron density and the H_2^+ photoionization rate as free parameters). Also shown in Fig. 1e is a simplified parameterization – "param 2", shown with crosses – where the heating rate Q_e is assumed to be a constant factor c of the H_2^+ photoionization rate $P_{H_2^+}$: $Q_e = cP_{H_2^+}$ ($c = 9 \times 10^{-12}$, Moore et al., 2008). This is the form of the standard parameterization applied in terrestrial TIGCMs (e.g., Roble et al., 1987; Millward et al., 1996). It can be seen from in Fig. 1e that, at least for Saturn, "param 1" represents a noticeable improvement over "param 2".

The ratio of the electron temperature calculated using the heating rate from the suprathermal electron code (T_e) over the electron temperature derived from "param 1" (T^*_e) is given in Fig. 2 for Run H. There is very good agreement overall between T_e and T^*_e. The mean ratio between the two temperature estimates over the entire daytime is 0.9995 (where the daytime is 06–19 LT here, as that is the period in which $T_e > T_n$ at Saturn). Electron densities are also affected slightly by changes in the plasma temperature (Moore et al., 2008), however, the difference in N_e induced by the use of T^*_e rather than T_e is only a fraction of a percent, and therefore not shown.

As the parameterization of the thermal electron heating rate was originally developed for one specific set of conditions (Moore et al., 2008), it is worthwhile to test that it applies equally well when the latitude, season, and solar flux have changed. These results are tabulated in Table 2, from which it can be seen that the parameterization of the thermal electron heating rate is able to reproduce electron temperatures calculated using the suprathermal electron code to within 2% on average across at least 30° of latitude, throughout the entire Saturn year, and over a complete solar cycle. The maximum deviation of T^*_e from T_e is ~12%, for Run C, and even in that case the discrepancy is localized to 1 Saturn hour and spans only ~100 km in altitude. Therefore, the parameterization works well over a wide range of latitudes, seasons, and solar cycles at Saturn. Also shown in Table 2 is the effect of the parameterization of the thermal electron heating rate on electron densities. The ratio of N_e from the full thermal balance calculations over N^*_e calculated using "param 1" for the heating

Table 1
Simulation conditions.

Run	Latitude (°)	Declination (°)	Solar flux	Solar cycle[a]
A	30	2.7	TIMED/SEE	Min
B	60	2.7	TIMED/SEE	Min
C	30	−26.73	TIMED/SEE	Min
D	30	2.7	TIMED/SEE	Max
E	30	2.7	Solar2000[b]	Max
F	30	2.7	EUVAC	Max
G	30	0	TIMED/SEE	Min
H	30	0	TIMED/SEE	Max

[a] Solar maximum fluxes are from 20 October, 2002, for which F10.7 was 180, and the Sun–Saturn distance was 9.03 AU. Solar minimum fluxes are from 15 May, 2008, for which the F10.7 was 70, and the Sun–Saturn distance was 9.30 AU.
[b] Solar2000 v2.33 was used.

Table 2
Effectiveness of thermal electron heating rate parameterization.

Run	Min T_e/T^*_e	Max T_e/T^*_e	Mean T_e/T^*_e	Min N_e/N^*_e	Max N_e/N^*_e	Mean N_e/N^*_e
A	0.933	1.04	1.02	0.9962	1.011	1.002
B	0.923	1.05	1.01	0.9926	1.020	1.002
C	0.880	1.06	1.01	0.9887	1.014	1.002
D	0.966	1.02	0.995	0.9907	1.003	0.9990
E	0.967	1.02	0.995	0.9902	1.003	0.9989
F	0.965	1.02	0.994	0.7543	1.061	0.9864
G	0.922	1.08	1.02	0.9387	1.013	1.003
H	0.912	1.04	1.00	0.9862	1.007	0.9995

Note: The minima, maxima, and means are taken between 06 and 19 LT in order to not contaminate the average with nighttime hours (where $T_e = T_n$, and therefore the ratio there is always equal to one).

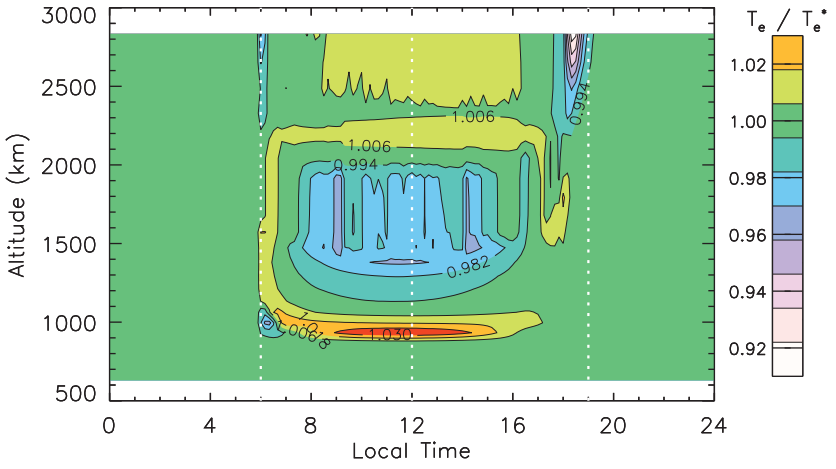

Fig. 2. Contours of the ratio of electron temperatures calculated with and without a parameterization of the thermal electron heating rate (Run H). The electron temperature T_e from a full transport calculation is divided by the electron temperature derived from "param 1" T^*_e (see text). The green color represents a ratio of 1 – i.e., excellent agreement. (For interpretation of the references to colour in this figure legend, the reader is referred to the web version of this article.)

rate is at all times close to one, indicating that there is essentially no difference introduced into calculations of electron density when the thermal electron heating rate is parameterized. Note that the findings presented in Fig. 2 and Table 2 result from simulations that account for both thermal electron heating and secondary production.

3.2. Secondary ionization: accuracy of parameterization

The parameterization of the secondary ion production rate is based on the ratio between the secondary production rate S and the primary production rate P. This ratio η, also known as secondary ionization efficiency, varies with time t, altitude z, and species s: $\eta_s(t, z)$. Rather than relying on the full 2D array of local time and altitude values of η, we have chosen to parameterize the ionization efficiency by fitting a power law for each of the main ionized constituents (i.e., H^+, H_2^+, and He^+) to the average η value between 08 and 16 LT – the daytime hours where secondary production is most important – giving $\eta_{avg}(z)$. Different forms of $\eta_{avg}(z)$ were also tested in which the local times averaged over varied from 00–24 LT to 12–12 LT; the hours of 08–16 provided the closest fit. Finally, a local time variation was reintroduced by comparing the known value of η calculated within the suprathermal electron routine with $\eta_{avg}(z)$. The final forms of the parameterization – $\eta_{H^+}(t,z)$, $\eta_{H_2^+}(t,z)$, and $\eta_{He^+}(t,z)$ – are given in Appendix A.

A demonstration of the effectiveness of the parameterization of the secondary production rate is given in Fig. 3, which plots the ratio of electron density calculated using the secondary production rates from the suprathermal electron code N_e over electron density calculated using the parameterized secondary production rate N^*_e. A noticeable deviation ($\leqslant$25%) between N_e and N^*_e is present near dawn; however, the parameterization does very well near noon, where the bulk of secondary production occurs.

As with the parameterization of the thermal electron heating rate, it is worthwhile to assess the accuracy of the parameterization for different latitudes, seasons, and solar fluxes. These results are tabulated in Table 3. On average, the parameterization of the secondary production rate is able to reproduce the electron density from the full suprathermal electron calculations to within 9%. There is one set of conditions, Run F that produces an outlier to this trend. Run F uses the EUVAC model to specify solar flux, so the increased importance of secondary production in Run F is indicative of an enhancement in the soft X-ray flux, which also causes the secondary ionization parameterization to lose accuracy. The parameterization is accurate to within 4% on average if Run F is discarded. Also shown in Table 3 is the minor effect of the parameterization of secondary ionization on electron temperature. Thus, T_e is the electron temperature from a simulation that includes the full electron transport calculation, while T^*_e comes from a simulation in which the secondary production rate is parameterized but the thermal electron heating rate is not.

3.3. Secondary ionization: importance at Saturn

A detailed study of the effects of primary and secondary ion production at Saturn is presented by Galand et al. (2009). Their calculations correspond to the conditions in Run G. They show that secondary production can lead to an enhancement of the peak electron density by as much as 30%, with significantly larger enhancements in the electron density of the lower ionosphere. In addition, by accounting for secondary production, the topside electron temperature is reduced by ~4% due to the fact that the same amount of energy is dispersed among a larger number of electrons (Moore et al., 2008).

In Table 4, we show T_e and N_e ratios between model simulations that do include secondary ionization and simulations that do not. Note that the model runs in Table 4 use the heating rate derived from a full transport calculation, Q_e. Table 4 demonstrates that the results of Galand et al. (2009) are roughly constant for a wide range of latitudes, Saturn seasons, and solar

Table 3
Effectiveness of secondary production rate parameterization.

Run	Min T_e/T^*_e	Max T_e/T^*_e	Mean T_e/T^*_e	Min N_e/N^*_e	Max N_e/N^*_e	Mean N_e/N^*_e
A	0.997	1.01	1.00	0.824	1.09	0.994
B	0.994	1.00	0.998	0.861	1.22	1.07
C	0.988	1.00	0.997	0.971	1.32	1.11
D	0.997	1.01	1.00	0.825	1.23	1.02
E	0.997	1.01	1.00	0.824	1.21	1.02
F	0.991	1.01	0.999	0.942	8.84	1.42
G	0.996	1.01	0.999	0.868	1.09	1.01
H	0.996	1.01	1.00	0.870	1.23	1.04

Note: The minima, maxima, and means are taken between 08 and 16 LT and 600–1500 km in order to focus on the regions where secondary production is most important.

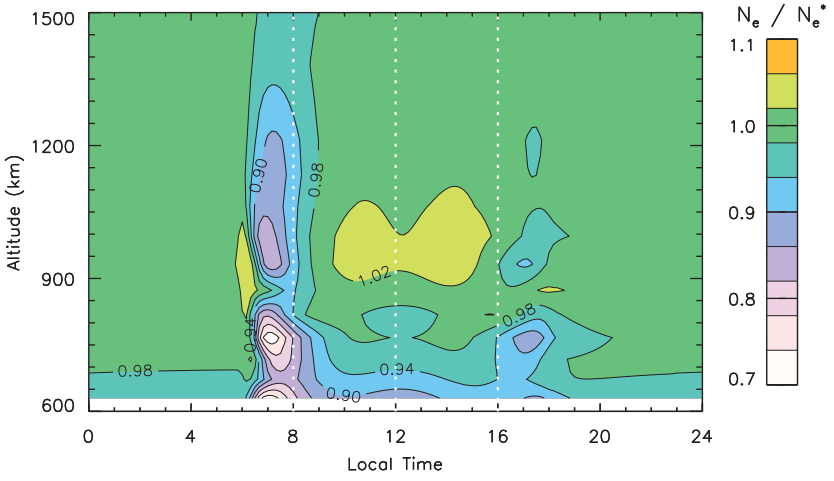

Fig. 3. Contours of the ratio of electron densities calculated with and without a parameterization of the secondary production rate (Run G). The electron density N_e from a full transport calculation is divided by the electron density derived from $\eta(z, t)$, N^*_e (see text). The green color represents a ratio of 1 – i.e., excellent agreement. (For interpretation of the references to colour in this figure legend, the reader is referred to the web version of this article.)

Table 4
Importance of secondary production at Saturn.

Run	Min T_{eSI}/T_e	Max T_{eSI}/T_e	Mean T_{eSI}/T_e	Min N_{eSI}/N_e	Max N_{eSI}/N_e	Mean N_{eSI}/N_e
A	0.966	1.00	0.985	1.09	8.10	2.06
B	0.966	1.00	0.983	1.12	8.59	2.31
C	0.958	1.05	0.987	1.12	8.98	2.32
D	0.964	1.00	0.984	1.09	9.28	2.07
E	0.964	1.00	0.984	1.09	8.02	2.06
F	0.945	1.01	0.983	1.10	33.0	3.78
G	0.958	1.00	0.984	1.09	8.78	2.07
H	0.955	1.00	0.983	1.09	10.1	2.07

Note: The minima, maxima, and means are taken between 08 and16 LT as the effects of secondary production are most pronounced during daytime hours. For T_e ratios, the entire altitude range shown in Fig. 1 is considered, while only 600–1500 km is considered for N_e ratios.

fluxes. In other words, the introduction of secondary ionization into calculations of Saturn's ionosphere reduces the average calculated plasma temperature by ~2%, and increases the mean electron density of the ionosphere below 1500 km by a factor of ~2. The one noticeable outlier to the general trend present in Table 4, Run F, is due to an enhancement in the EUVAC soft X-ray flux, as discussed in Section 3.2.

4. Summary

Solar EUV and X-ray radiation is absorbed in Saturn's (mostly) hydrogen atmosphere predominantly below 2000 km altitude, driving a host of important processes in the thermosphere and ionosphere. Recently, the effects of thermal electron heating (Moore et al., 2008) and secondary ion production (Galand et al., 2009) have been explored in Saturn's mid-latitude ionosphere. In this paper, we have developed a parameterization of the secondary ionization efficiency η from self-consistent calculations, and we have investigated the accuracy of the parameterization of the thermal electron heating rate (Moore et al., 2008) and of η over a range of latitudes, seasons, and solar flux inputs.

While secondary ionization has been accounted for at Earth (Schlesier and Buonsanto, 1999), Mars (Fox and Yeager, 2006), Venus (Fox, 2007), and Jupiter (Kim and Fox, 1994), the majority of secondary ionization studies have been in 1D. Secondary ionization in non-terrestrial TIGCMs (i.e., 3D models) and at Saturn has been neglected for the most part. On average, we show here that secondary ionization by electron impact at Saturn can account for an increase in low-altitude electron densities by a factor of 2 (with a maximum increase of ~10), and it can enhance the peak electron density by as much as 30% (Galand et al., 2009). In addition, calculations of electron temperature at Saturn that do not include secondary ionization will overestimate T_e by ~2% on average. We have developed a parameterization of the secondary ionization rate that is accurate to within ~4% for solar fluxes spanning a solar cycle, for Saturn solstice and equinox, and across 30° of latitude. Such a parameterization can provide a reasonable approximation of this important process in global models – such as the STIM TIGCM (Mueller-Wodarg et al., 2006) – which seek to simulate the entire upper atmosphere of Saturn in a coupled, self-consistent manner.

By evaluating the effectiveness of the parameterization of the thermal electron heating rate Q^*_e developed in Moore et al. (2008) over a wide range of conditions, we have demonstrated here that it too is capable of providing a reasonable approximation to a complex process within a more comprehensive model. On average, the ion and electron temperatures that result from the application of Q^*_e is within 2% of the result from the full transport calculation, independent of incident flux, Saturn season, or latitude.

The makeup of Saturn's upper atmosphere and the photochemistry of its ionosphere are similar in the other giant planets, and likely at many exoplanets as well. Therefore, where previous studies are unavailable, the good accuracy of the two parameterizations evaluated here over a wide range of solar and seasonal conditions gives some confidence that they may be applied at other planets as a first approximation to those ionospheres.

Acknowledgements

We are very grateful to the TIMED/SEE PI, Tom Woods, and his team for providing us with the solar flux dataset and associated routines for extrapolation to planets. Solar Irradiance Platform historical irradiances are provided courtesy of W. Kent Tobiska and Space Environment Technologies. These historical irradiances have been developed with partial funding from the NASA UARS, TIMED, and SOHO missions. Funding for this work at Boston University comes, in part, from the NASA CDAP Program (LM), the Planetary Atmospheres Program (MM, MG), and from the Center for Space Physics. In addition, MG was partially supported by the STFC rolling grant awarded to Imperial College London.

Appendix A

The parameterization of the thermal electron heating rate is described by Moore et al. (2008). It is defined as follows:

$$Q_e(z,t) = (10^{-12}\,\mathrm{erg})c(z)P_{H_2^+}(z,t)\left[1+\frac{N_{e,noon}(z)}{10^3\,\mathrm{cm}^{-3}}\right],\ \mathrm{erg\,cm^{-3}\,^{-1}}, \tag{A1}$$

where $P_{H_2^+}$ is the primary photoionization rate of H_2^+ in $\mathrm{cm^{-3}\,s^{-1}}$, $N_{e,noon}$ the electron density at noon in $\mathrm{cm^{-3}}$, and c is a dimensionless parameterization constant whose value varies with altitude,

$$c = \begin{cases} 1.0 & z \leqslant 1800\,\mathrm{km} & p \geqslant 5.3\times10^{-6}\,\mathrm{mbar} \\ 1.2 & 1800\,\mathrm{km} < z \leqslant 2300\,\mathrm{km} & 5.3\times10^{-6} > p \geqslant 3.4\times10^{-7}\,\mathrm{mbar} \\ 1.5 & 2300\,\mathrm{km} < z \leqslant 2600\,\mathrm{km} & 3.4\times10^{-7} > p \geqslant 6.5\times10^{-8}\,\mathrm{mbar} \\ 2.25 & z > 2600\,\mathrm{km} & 6.5\times10^{-8} > p\,\mathrm{mbar} \end{cases}. \tag{A2}$$

The parameterizations of the secondary ion production rates depend on a function of local time, $b(t)$

$$b(t) = 1 + 0.0022|t-12|^4, \tag{A3}$$

where t is the local time in Saturn hours (normalized to 24). For example, at 10:48 AM Saturn local time, t has a value of 10.8, and $b(t)$ is ~1.005. At Saturn, the total ion production rate for H^+, H_2^+, and He^+ can be derived from the respective primary production rates by applying the following secondary ionization efficiencies,

$$\begin{aligned} \eta_{H^+}(t,z) &= b(t)(8.77\times10^{26}z^{-9.347} + 44.29z^{-0.8973}) \\ \eta_{H_2^+}(t,z) &= b(t)(1.70\times10^{22}z^{-7.49} + 3.515\times10^{8}z^{-2.9464}), \\ \eta_{He^+}(t,z) &= b(t)(3.84\times10^{17}z^{-6.4223} + 4.463z^{-0.877}), \end{aligned} \tag{A4}$$

where z is the altitude above Saturn's 1 bar pressure level in km. For example, at 10:48 AM Saturn time, $\eta_{H_2^+}$ is 1.09 at 1000 km, meaning photoionization of H_2 alone accounts for almost half of the total H_2^+ ion production rate (the remainder being due to photoelectron and secondary electrons). Alternatively, if applying the parameterization of the ionization efficiencies to an atmosphere different than the Saturn one given in Fig. 1 of Moore et al.

(2008), it is best to use pressure coordinates,

$$\eta_{H^+}(t,p) = b(t)(24.00p^{0.7950} + 0.2155p^{0.08894})$$
$$\eta_{H_2^+}(t,p) = b(t)(64.87p^{0.5816} + 1.25p^{0.3332}),$$
$$\eta_{He^+}(t,p) = b(t)(1.221p^{0.4915} + 0.0304p^{0.0812}), \quad \text{(A5)}$$

where p is the pressure in Pa.

References

Achilleos, N., Miller, S., Tennyson, J., Aylward, A.D., Mueller-Wodarg, I., Rees, D., 1998. JIM: a time-dependent, three-dimensional model of Jupiter's thermosphere and ionosphere. J. Geophys. Res. 103, 20089–20112.

Atreya, S.K., Waite, J.H., Donahue, T.M., Nagy, A.F., McConnell, J.C., 1984. Theory, measurements and models of the upper atmosphere and ionosphere of Saturn. In: Gehrels, E. (Ed.), Saturn. University of Ariz. Press, Tucson, pp. 239–277.

Bougher, S.W., Waite Jr., J.H., Majeed, T., Gladstone, G.R., 2005. Jupiter thermospheric general circulation model (JTGCM): global structure and dynamics driven by auroral and Joule heating. J. Geophys. Res. 110, E04008.

Connerney, J.E.P., Waite Jr., J.H., 1984. New model of Saturn's ionosphere with an influx of water from the rings. Nature 312, 136–138.

Cowley, S.W.H., Arridge, C.S., Bunce, E.J., Clarke, J.T., Coates, A.J., Dougherty, M.K., Grodent, D., Nichols, J.D., Talboys, D.L., 2008. Auroral current systems in Saturn's magnetosphere: comparison of theoretical models with Cassini and HST observations. Ann. Geophys. 26, 2613–2630.

Fox, J.L., Yeager, K.E., 2006. Morphology of the near-terminator Martian ionosphere: a comparison of models and data. J. Geophys. Res. 111, A10309.

Fox, J.L., 2007. Near-terminator Venus ionosphere: how chapman-esque? J. Geophys. Res. 112, E04S02.

Galand, M., Moore, L., Charnay, B., Mueller-Wodarg, I., Mendillo, M., 2009. Modeling the photoelectron secondary ionization process at Saturn, accepted. J. Geophys. Res., doi:10.29/2008JA013981

Heroux, L., Higgins, J.E., 1977. Summary of full dusk solar fluxes between 250 and 1940 Å. J. Geophys. Res. 82, 3307.

Hinteregger, H.E., Fukui, K., Gilson, B.R., 1981. Observational, reference and model data on solar EUV, from measurements on AE-E. Geophys. Res. Lett. 8, 1147.

Hubbard, W.B., Porco, C.C., Hunten, D.M., Rieke, G.H., Rieke, M.J., McCarthy, D.W., Haemmerle, V., Haller, J., McLeod, B., Lebofsky, L.A., Marcialis, R., Holberg, J.B., landau, R., Carrasco, L., Elias, J., Buie, M.W., Dunham, E.W., Persson, S.E., Boroson, T., West, S., French, R.G., Harrington, J., Elliot, J.L., Forrest, W.J., Pipher, J.L., Stover, R.J., Brahic, A., Grenier, I., 1997. Structure of Saturn's mesosphere from the 28 SGR occultations. Icarus 130, 404–425.

Huestis, D.L., 2008. Hydrogen collisions in planetary atmospheres, ionospheres, and magnetospheres. Plan. Space Sci. 56, 1733–1743.

Johnson, R.E., Smith, H.T., Tucker, O.J., Liu, M., Burger, M.H., Sittler, E.C., Tokar, R.L., 2006. The Enceladus and OH tori at Saturn. Astrophys. J. 644, L137–L139.

Jurac, S., Richardson, J.D., 2005. A self-consistent model of plasma and neutrals at Saturn: neutral cloud morphology. J. Geophys. Res. 110, A09220.

Kim, Y.H., Fox, J.L., 1994. The chemistry of hydrocarbon ions in the Jovian ionosphere. Icarus 112, 310–325.

Kliore, A.J., Nagy, A.F., Marouf, E.A., Anabtawi, A., Barbinis, E., Fleischman, D.U., Kahane, D.S., 2009. Midlatitude and high-latitude electron density profiles in the ionosphere of Saturn obtained by Cassini radio occultation observations. J. Geophys. Res., 114, A04315, doi:10.1029/2008JA013900

Lilensten, J., Kofman, W., Wisemberg, J., Oran, E.S., Devore, C.R., 1989. Ionization efficiency due to primary and secondary photoelectrons—A numerical model. Ann. Geophys. 7, 83–90.

Matcheva, K.I., Strobel, D.F., Flasar, F.M., 2001. Interaction of gravity waves with ionospheric plasma: implications for Jupiter's ionosphere. Icarus 152, 347–365.

McConnell, J.C., Holberg, J.B., Smith, G.R., Sandel, B.R., Shemansky, D.E., Broadfoot, A.L., 1982. A new look at the ionosphere of Jupiter in light of the UVS occultation results. Planet. Space Sci. 30, 151–167.

McElroy, M.B., 1973. The ionospheres of the major planets. Space Sci. Rev. 14, 460–473.

Mendillo, M., Moore, L., Clarke, J., Mueller-Wodarg, I., Kurth, W.S., Kaiser, M.L., 2005. Effects of ring shadowing on the detection of electrostatic discharges at Saturn. Geophys. Res. Lett. 32, L05107.

Miller, S., Aylward, A., Millward, G., 2005. Giant planet ionospheres and thermospheres: the importance of ion–neutral coupling. Space Sci. Rev. 116, 319–343.

Millward, G.H., Moffett, R.J., Quegan, W., Fuller-Rowell, T.J., 1996. A coupled thermospheric–ionospheric–plasmasphere model (CTIP). In: Schunk, R.W. (Ed.), STEP: Handbook of Ionospheric Models. Utah State Univ., Logan, Utah, p. 173.

Moore, L.E., Mendillo, M., Mueller-Wodarg, I.C.F., Murr, D.L., 2004. Modeling of global variations and ring shadowing in Saturn's ionosphere. Icarus 172, 503–520.

Moore, L., Nagy, A.F., Kliore, A.J., Mueller-Wodarg, I., Richardson, J.D., Mendillo, M., 2006. Cassini radio occultations of Saturn's ionosphere: model comparisons using a constant water flux. Geophys. Res. Lett. 33, L22202.

Moore, L., Mendillo, M., 2007. Are depletions in Saturn's ionosphere caused by explosive surges of water from Enceladus? Geophys. Res. Lett. 34, L12202.

Moore, L., Galand, M., Mueller-Wodarg, I., Yelle, R.V., Mendillo, M., 2008. Plasma temperatures in Saturn's ionosphere. J. Geophys. Res. 113, A10306.

Moses, J.I., Bezard, B., Lellouch, E., Gladstone, G.R., Feuchtgruber, H., Allen, M., 2000a. Photochemistry of Saturn's atmosphere, I, hydrocarbon chemistry and comparisons with ISO observations. Icarus 143, 244–298.

Moses, J.I., Lellouch, E., Bézard, B., Gladstone, G.R., Feuchtgruber, H., Allen, M., 2000b. Photochemistry of Saturn's atmosphere, II. Effects of an influx of external oxygen. Icarus 145, 166–2002.

Moses, J.I., Bass, S.F., 2000. The effects of external material on the chemistry and structure of Saturn's ionosphere. J. Geophys. Res. 105, 7013–7052.

Mueller-Wodarg, I.C.F., Mendillo, M., Yelle, R.V., Aylward, A.D., 2006. A global circulation model of Saturn's thermosphere. Icarus 180, 147–160.

Nagy, A.F., Kliore, A.J., Marouf, E., French, R., Flasar, M., Rappaport, N.J., Anabtawi, A., Asmar, S.W., Johnston, D., Barbinis, E., et al., 2006. First results from the ionospheric radio occultations of Saturn by the Cassini spacecraft. J. Geophys. Res. 111, A06310.

Porco, C.C., et al., 2006. Cassini observes the active South pole of Enceladus. Science 311, 1393–1401.

Richards, P.G., Torr, D.G., 1988. Ratios of photoelectron to EUV ionization rates for aeronomic studies. J. Geophys. Res. 93, 4060–4066.

Richards, P.G., Fennelly, J.A., Torr, D.G., 1994a. EUVAC: a solar EUV flux model for aeronomic calculations. J. Geophys. Res. 99, 8981–8992.

Richards, P.G., Fennelly, J.A., Torr, D.G., 1994. Erratum: EUVAC: a solar EUV flux model for aeronomic calculations. J. Geophys. Res. 99, 8981–8992.Richards, P.G., Fennelly, J.A., Torr, D.G., 1994. J. Geophys. Res. 99, 13283–13284.

Roble, R.G., Ridley, E.C., Dickinson, R.E., 1987. On the global mean structure of the thermosphere. J. Geophys. Res. 92, 8745–8758.

Schlesier, A.C., Buonsanto, M.J., 1999. The Millstone hill ionospheric model and its application to the May 26–27, 1990, ionospheric storm. J. Geophys. Res. 104, 22,453–22,468.

Schunk, R.W., Nagy, A.F., 1978. Electron temperatures in the F region of the ionosphere: theory and observations. Rev. Geophys. Space Phys. 16, 355.

Smith, G.R., Shemansky, D.E., Holberg, J.B., Broadfoot, A.L., Sandel, B.R., McConnell, J.C., 1983. Saturn's upper atmosphere from the Voyager 2 EUV solar and stellar occultations. J. Geophys. Res. 88, 8667–8678.

Swartz, W.E., Nisbet, J.S., 1972. Revised calculations of F region ambient electron heating by photoelectrons. J. Geophys. Res. 77, 6251–6259.

Titheridge, J.E., 1996. Direct allowance for the effect of photoelectrons in ionospheric modeling. J. Geophys. Res. 101, 357–369.

Tobiska, W.K., Bouwer, S.D., 2006. New developments in Solar2000 for space research and operations. Adv. Space Res. 37, 347–358.

Tobiska, W.K., Woods, T., Eparvier, F., Viereck, R., Floyd, L., Bouwer, D., Rottman, G., White, O.R., 2000. The Solar2000 empirical solar irradiance model and forecast tool. J. Atmos. Sol. Terr. Phys. 62, 1233–1250.

Torr, M.R., Torr, D.G., Ong, R.A., Hinteregger, H.E., 1979. Ionization frequencies for major thermospheric constituents as a function of solar cycle 21. Geophys. Res. Lett. 6, 771.

Woods, T.N., Eparvier, F.G., Bailey, S.M., Chamberlin, P.C., Lean, J., Rottman, G.J., Solomon, S.C., Tobiska, W.K., Woodraska, D.L., 2005. The solar EUV experiment (SEE): mission overview and first results. J. Geophys. Res. 110, A01312.